Novel Perovskite Solar Cell Architecture Featuring Efficient Light Capture and Ultrafast Carrier Extraction

Yu Yu,[†,‡,§,#] Lei Lei,[†,‡,#] Songwang Yang,*,[‡] Junjie Xie,[‡] Jun Shao,[‡] Qipeng Cao,[‡] Sheng Zhang,[‡,||] Xiaojie Ni,[⊥] Bangjiao Ye,[⊥] and Yan Liu*,[†,‡]

[†]State Key Laboratory of High Performance Ceramics and Superfine Microstructures and [‡]CAS Key Laboratory of Materials for Energy Conversion, Shanghai Institute of Ceramics, Chinese Academy of Sciences, Shanghai 200050, P. R. China

[§]University of Chinese Academy of Sciences, Beijing 100039, P. R. China

[||]School of Environmental and Materials Engineering, College of Engineering, Shanghai Second Polytechnic University, Shanghai 201209, P. R. China

[⊥]State Key Laboratory of Particle Detection and Electronics, University of Science and Technology of China, Hefei 23006, P. R. China

S *Supporting Information*

ABSTRACT: A new perovskite solar cell (PSC) structure with a functionalized interface between perovskite and a hole transport material has been proposed in this report. The short circuit current density of PSC was notably enhanced with the novel architecture (with an increase of 8.7%), and a power conversion efficiency (PCE) of 16.93% was achieved. With the increased perovskite/hole conductor interface, hysteresis suppression was observed. The advantages of this structure in light-harvesting efficiency, trap density, and carrier separation rate were proved by various characterization and analysis studies. It is noteworthy that a PCE of 14.67% was achieved with poly(3-hexyl-thiophene), which to our knowledge is the highest performing PSC based on this material.

KEYWORDS: *perovskite solar cell, device architecture, light harvesting, carrier separation, transient photoluminescence spectroscopy*
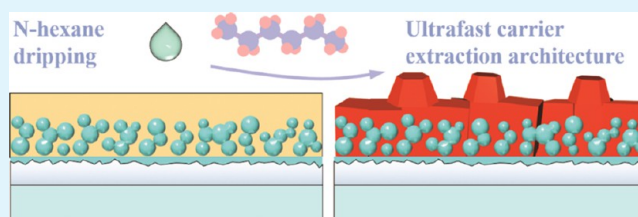
1. INTRODUCTION

Alkali lead halide perovskite APbX$_3$ (A = Cs$^+$, CH$_3$NH$_3^+$ (MA$^+$), and CH(NH$_2$)$_2^+$ (FA$^+$); X = I$^-$ and Br$^-$) is one of the most promising solar-to-electricity conversion materials. The power conversion efficiency (PCE) of perovskite solar cells (PSCs) soared from an initial value of 3.8[1]–22.1%[2] at an amazing speed with painstaking efforts. Peculiarities including a high light extinction coefficient,[3−8] nonpolar carrier mobility,[9−13] tunable band gap,[14−25] colorful appearance,[14,16,24−27] and low-temperature solution processability[5,8,28−35] have been verified for perovskite. With these properties, high PCE could be achieved with a simple solution process as well as considerably low consumption of materials and energy.

As the most investigated light absorber in perovskite solar devices, methylammonium lead iodide (MAPbI$_3$) has been prepared by various methods: one-step[5,8,28,30,35−40] and sequential deposition[7,29,41−45] methods have been developed in solution and in a vapor atmosphere. The strategy of the two-step sequential deposition is preparing a PbI$_2$ film and transforming it to perovskite in methylammonium iodide (MAI) either in solution or in a vapor state,[46] instead of directly mixing the precursors. The two-step deposition limits the reaction rate by controlling the diffusion speed of MAI at the perovskite/PbI$_2$ interface and yields a relatively uniform perovskite. Although grain size and morphology control are

convenient, the two-step technique is relatively complex and time-consuming. Besides, sequential deposition lacks the ability to fabricate perovskite with precise stoichiometry.

The one-step method emphasizes on mixing the precursors before or during the film forming process. In the vapor scheme, PbI$_2$ and MAI react in a gaseous state, wherein the vapor yields from heating boats in vacuum.[36] For the solution technique, the two components are dissolved in a solvent and spin-coated on substrates. The as-casted intermediate turns to perovskite during heat treatment. Various efforts have been made by researchers to prepare flat and homogeneous perovskite films with the one-step spin-coating process.[8,30,31,37] All these efforts aimed at matching the supersaturation level of PbI$_2$ and MAI, who have a high solubility disparity. The utilization of nonsolvents,[30,31,35] that is, solvents that barely or do not dissolve perovskite or its components at all, is impressive. The dripping of nonsolvents precipitate perovskite (intermediate) during spin coating. Dense nuclei of perovskite (intermediate) form and grow into well-defined grains. In addition, dimethyl sulfoxide (DMSO)[31,35,47] is introduced in the perovskite solution to enhance the film quality. This retards the

crystallization of perovskite by forming an intermediate, PbI_2·DMSO·MAI.[35]

With tremendous efforts and trials, the PCEs of PSCs on the basis of the one-step solution process was boosted from 9.7%[28] to over 20%.[18,25,48] To some extent, the improvement of the film fabrication technique contributes to the booming of perovskite photovoltaics. The one-step process is relatively simple, and the film properties can be tuned by changing the precursor ratio.[18,23,49] However, the product morphology is relatively less controllable.

To exert the photovoltaic performance of the perovskite light absorber to optimum, the carrier transport layer and device architecture are of vital significance. Here, a new PSC structure, the UFCEA, is designed and realized. The feature of UFCEA is the enlarged perovskite/hole transport material (HTM) interface, which notably enhances the carrier separation rate, as illustrated in Figure 1a. The perovskite film in UFCEA has a
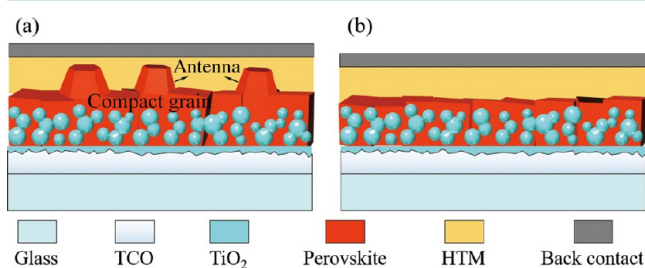
Figure 1. Illustration of (a) UFCEA and (b) the conventional structure of a perovskite solar device.

hierarchy structure with a compact layer and numerous nanoantennas. Compared with the traditional structure, UFCEA enhances the visible light capture by light scattering at the interface. Although the perovskite in UFCEA has a larger surface area, the defect density is low. With UFCEA, we achieved a PCE of 16.93% under optimized conditions. The short current density was remarkably increased compared to that in the traditional structure.

2. EXPERIMENTS AND METHODS

2.1. Experiments. The detailed fabrication process of solar cell devices is provided in the Supporting Information (SI). Perovskite films in both structures were fabricated with a precursor solution containing 0.6915 g mL^{-1} PbI_2, 0.2385 g mL^{-1} MAI, and 212.7 μL mL^{-1} DMSO, with dimethylformamide (DMF) as the solvent. For the traditional structure, a reported approach was used. In brief, 0.5 mL of ethyl ether was dripped on the precursor solution at the seventh second after the start of spin coating (5000 rpm/20 s). The morphology design of perovskite in UFCEA was realized by an elaborate control of the crystallization process. As MAI is sensitive to numerous polar solvents, only weak polar solvents and nonpolar solvents are suitable to precipitate and crystallize perovskite. In this work, n-hexane was used to tune the crystallization process and form a perovskite film with a rough surface. In detail, the precursor solution was spin coated on mesoporous TiO_2 at 5000 rpm for 20 s. A volume of 0.5 mL of n-hexane was dripped continuously for 6 s from the seventh second after substrate rotation. The film surface immediately turned blur upon coming in contact with the n-hexane flow. The perovskite films were prepared in a dry room where the room temperature and relative humidity were controlled at 20 °C and less than 1%, respectively.

2.2. Methods. The top view morphology of the perovskite films as well as the cross-section of different device architectures were investigated using a field emission scanning electron microscope (FESEM) (FEI, Magellan 400). The perovskite phase was identified by

X-ray diffraction (XRD) measurement with an Ultima IV X-ray diffractometer using Cu Kα radiation (step width: 0.02; scan speed: 4°/min). The grain size statistics were obtained from scanning electron microscopy images by measuring the horizontal length of perovskite grains.

The visible−near infrared (vis−NIR) absorbance spectra of different perovskite films were recorded on a vis−NIR spectrophotometer (HITACHI U-3010). The optical band gaps of the perovskite films in UFCEA and the normal structure were calculated by extrapolating the absorption edge in Tauc's plot. The figure was plotted according to Tauc's law: $(\alpha h\nu)^2 \sim h\nu - E_g$, where α is the absorption coefficient, $h\nu$ is the photon energy, and E_g is the band gap. On the basis of the absorbance spectra, light-harvesting efficiencies (LHEs) were calculated according to the following equation

$$LHE = 1 - 10^{-A_b} \tag{1}$$

where A_b is the absorbance of the perovskite films at different wavelengths.

The positron annihilation spectra (PAS) were obtained with a slow positron beam spectrometer developed by State Key Laboratory of Particle Detection and Electronics, University of Science and Technology of China. The Doppler broadening spectrum measures the γ-ray intensity emitted during the annihilation between electrons and positrons. The energy of the incident positron beam is continuously tunable between 0 and 20 keV. Linear parameters S and W were used to reveal the variation of the Doppler broadening spectra due to the low energy resolution. The S-parameter is defined as the center area (0.511 MeV)/total peak area ratio. W is the ratio of the counts between the side area and total peak area. When a positron is captured by a defect, the annihilation probability with a high-momentum core electron decreases. As a result, the S-parameter increases, whereas the W-parameter decreases. For this reason, the S-parameter is also known as the low-momentum annihilation fraction and reflects the information of low-momentum electrons, such as valance electrons and free electrons in the conduction band for instance. As for the W-parameter, it reflects the information of high-momentum electrons, namely core electrons, and is named high-momentum annihilation fraction. The PL intensity of perovskite films were measured (FluoroMax-4; HORIBA, Ltd.) with the excitation wavelength fixed at 566 nm. The slit widths for both the incident light and the emission signal were 5 mm. Time-resolved PL spectra were obtained using a fluorescence lifetime spectrometer (Photo Technology International, Inc.). The intensity decay of fluorescence at 765 nm was tracked with a picosecond resolution. The PL decay data were fitted with the triexponential model: $I = I_0 + A_e \exp(-t/\tau_e) + A_h \exp(-t/\tau_h) + A_0 \exp(-t/\tau_0)$, where t, I, I_0, τ_e, A_e, τ_h, A_h, τ_0, and A_s are decay time, PL intensity at t, initial PL intensity, decay lifetime caused by electron extraction, electron extraction lifetime coefficient, decay lifetime caused by hole extraction, hole extraction lifetime coefficient, decay lifetime of recombination, and self-consumption coefficient. The average lifetime, τ_{ave}, was calculated according to the fitting results

$$\tau_{ave} = \frac{A_e \tau_e^2 + A_h \tau_h^2 + A_0 \tau_0^2}{A_e \tau_e + A_h \tau_h + A_0 \tau_0} \tag{2}$$

Current density−voltage ($J-V$) characteristics of UFCEA and normal structure PSCs were measured under simulated AM 1.5G illumination with the effective area fixed at 0.07 cm^2. The bias range of the $J-V$ test was 0−1.1 V with a voltage step of 0.002 V. The hold time before measuring the current at each voltage step was 50 ms, and the time interval between steps was 10 ms. The light intensity was calibrated with a reference silicon solar cell (Oriel 91150). The PCE histograms of devices with different structures were obtained by testing 12 individual cells in one batch. The stability of the cells was obtained by testing the $J-V$ curves of devices after a certain storage time in the dark in a dry room (room temperature 20 °C, relative humidity <1%). $J-V$ hysteresis was checked by measuring the current responses to an increasing bias from 0 to 1.1 V (forward scan) and a decreasing bias from 1.1 to 0 V (reverse scan). The hysteresis index (HI) was calculated according to the following equation[24]
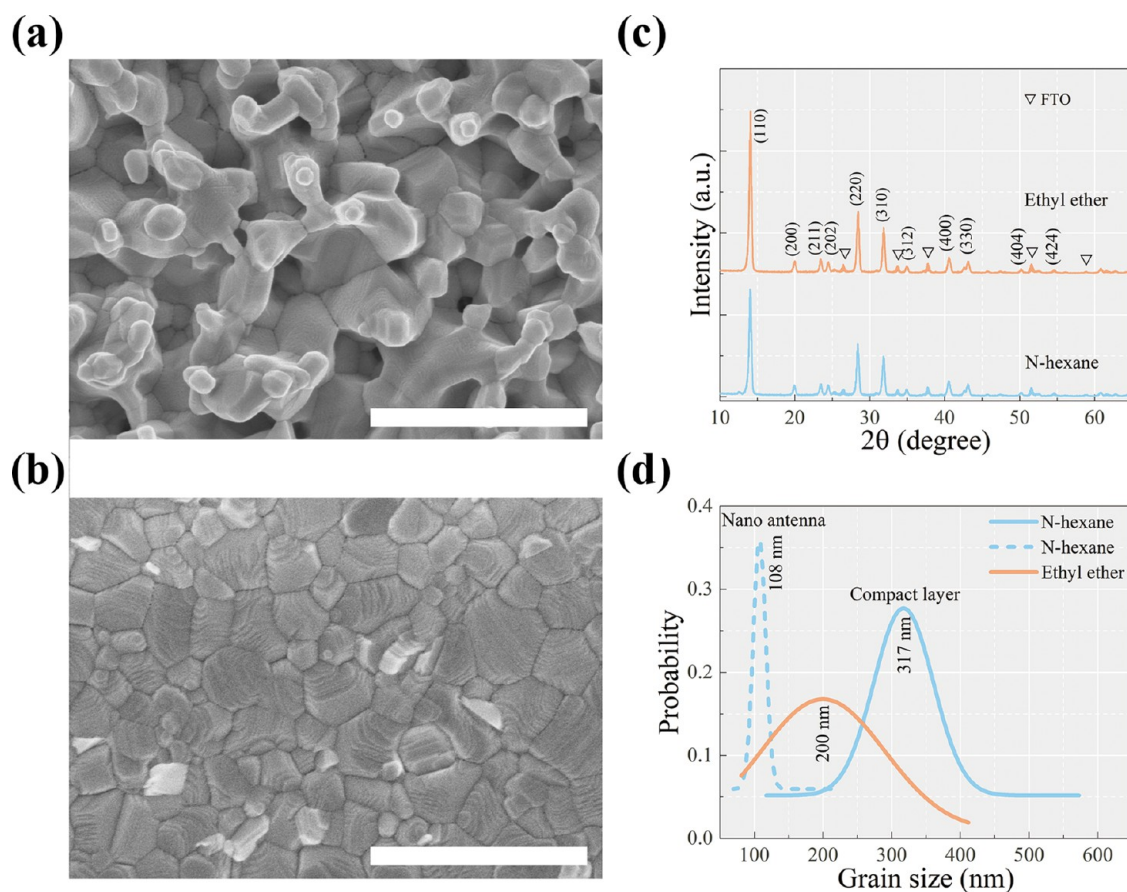
Figure 2. FESEM top-view morphology of perovskite prepared by (a) *n*-hexane and (b) ethyl ether dripping, the scale bars are 1 *μ*m. (c) XRD patterns of perovskite prepared by *n*-hexane dripping as well as ethyl ether. (d) Statistic of grain sizes of perovskite prepared by *n*-hexane dripping as well as ethyl ether.

$$\text{HI} = \frac{\int_0^{V_{OC,R}} J_R \, dV - \int_0^{V_{OC,F}} J_F \, dV}{\int_0^{V_{OC,R}} J_R \, dV} \times 100\%$$

(3)

where $V_{OC,R}$ and $V_{OC,F}$ are the open circuit voltages of reverse and forward scans and J_R and J_F are the current densities for reverse and forward scans, respectively. For both UFCEA and normal structure PSCs, HI statistics were obtained on the basis of the forward and reverse scan *J*−*V* curves of eight cells.

Maximum power point tracking was conducted with a CHI 660C electrochemical station (ALS Co., Ltd.). The current output under the voltage at the maximum power point was recorded for 120 s. The incident photon-to-current conversion efficiency (IPCE) was measured with an SM-250 system (Bunkoh-keiki Co., Ltd., Japan). The intensity of monochromatic light was calibrated with a Si photodiode (S1337-1010BQ).

3. RESULTS AND DISCUSSION

3.1. Phase and Morphology. The top-view FESEM morphology and XRD patterns of perovskite prepared with *n*-hexane and ethyl ether dripping on top of a mesoporous TiO$_2$ scaffold are presented in Figure 2. For both samples, the grain boundaries are clear and distinct, indicating the formation of well-crystallized grains. The peculiarity of the porous and rough surface of the *n*-hexane-dripped perovskite film in contrast with the smooth and dense ethyl ether counterpart is graphically presented. The *n*-hexane-dripped sample developed a hierarchy structure: nanostructures erecting on compact grains. The compact and densely packed perovskite grains are of vital

significance in UFCEA to insulate HTM from mesoporous TiO$_2$ and thus avoid serious recombination.

The formation of a tetragonal perovskite phase by one-step spin coating with dripping of different nonsolvents was verified by XRD (Figure 2c). The characteristic peak at 14.28° corresponding to the diffraction of the (110) lattice plane of perovskite was perfectly detected, whereas no signal of PbI$_2$ was observed. The main peak intensity of the *n*-hexane-dripped perovskite film is slightly weaker than that of the ethyl ether-dripped sample. The reason lies in the porous surface of *n*-hexane, which decreases the X-ray exposure volume of the perovskite grains.

The grain sizes of the perovskite films are estimated according to the FESEM pictures, and the statistics are presented in Figure 2d. The perovskite grains prepared with ethyl ether dripping are distributed around 200 nm. In UFCEA, the perovskite layer is specialized as a compact light-absorbing layer that ensures sufficient light capture and nanoantennas that enhance the carrier extract rate at the perovskite/HTM interface. For the *n*-hexane-dripped sample, the compact perovskite has a most probable grain size of about 317 nm, whereas the value of nanoantennas is near 108 nm. The grain size of the compact layer in the *n*-hexane-dripped sample is larger than that of the ethyl ether sample, which ensures superior photovoltaic properties. The larger grain size in the compact layer of the *n*-hexane-dripped sample could also be easily noticed by the fact that less grains are spotted in the same area.
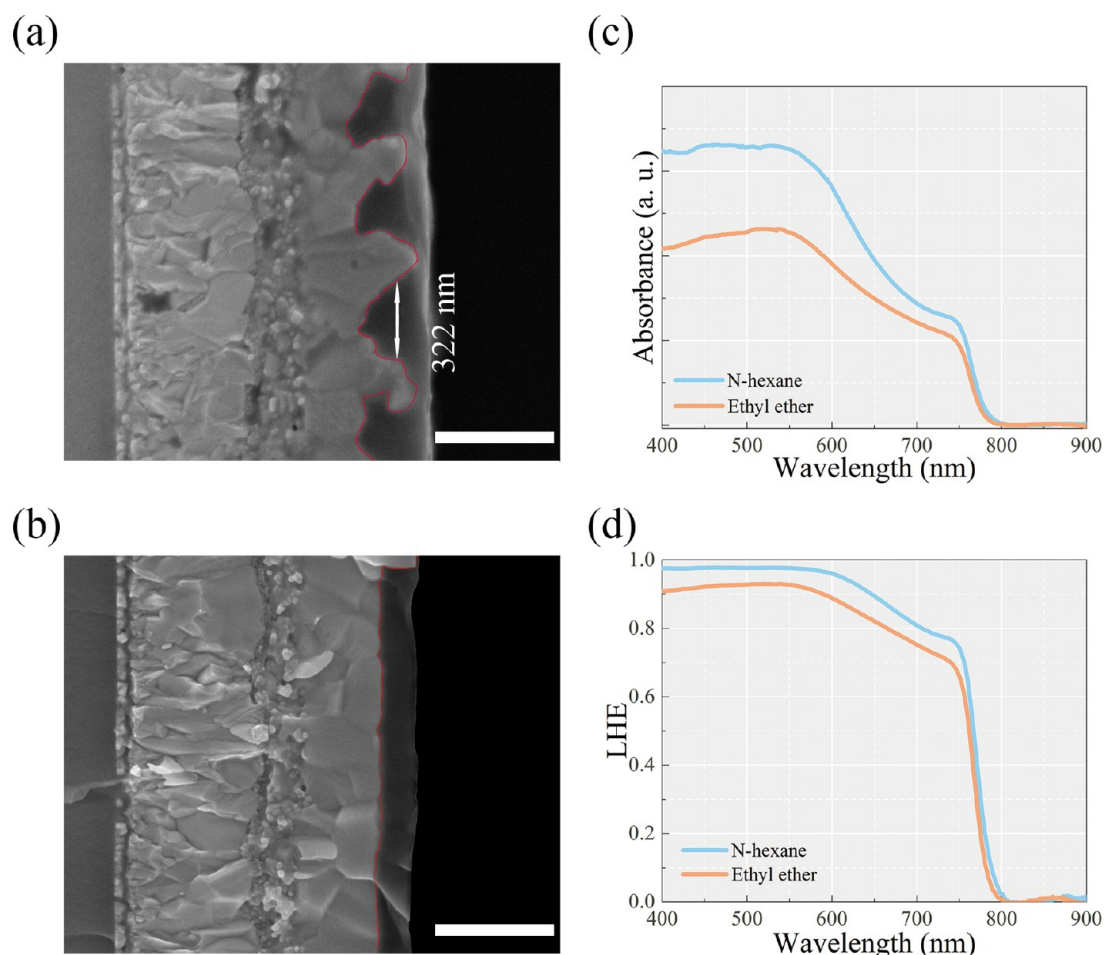
Figure 3. Cross-section of (a) UFECA and (b) conventional structure, the scale bars in this figure are 500 nm. (c) Vis−NIR absorption spectra and (d) light-harvesting efficiency (LHE) of perovskite on top of the mesoporous scaffold prepared by dripping of different nonsolvents.

3.2. Light Capture Analysis. The cross-section FESEM morphology of HTM-coated perovskite films prepared by dripping of different nonsolvents is shown in Figure 3a,b. In contrast with the ethyl ether-dripped sample, the n-hexane-dripped perovskite has a wave-shaped contact with HTM; red lines are drawn to aid the eyes (Figure 3a). The half-height width of the nanoantennas and half-depth width of the valleys are distributed around 200−300 nm. They have the same scale with the wavelength of visible light and hence would have a scattering effect. As presumed, the light absorbance of the effective material in UFCEA was notably enhanced, as shown in the vis−NIR absorption spectra in Figure 3c. The $(\alpha h\nu)^2 - h\nu$ relation was plotted according to Tauc's rule (Tauc's plot, Figure S1). The optical band gaps of the perovskite films prepared by n-hexane and ethyl ether nonsolvents were estimated to be 1.61 eV. The LHEs of the perovskite films in different device structures were plotted as presented in Figure 3d. LHE denotes the percentage of light absorbed by perovskite at a certain wavelength. As presented in Figure 3d, the LHE of perovskite film in different cell structures have a similar trend. With the decrease in wavelength, the LHEs sharply increase at 800 nm and reach a plateau at about 600 nm. However, the perovskite film in UFCEA has a higher LHE value through the available spectra. As mentioned above, the textured perovskite/HTM interface at the hundred nanometer scale would conspicuously enhance the light utilization for the light scattering effect.

3.3. Defect Analysis. The defect and interface status of UFCEA and the normal structure were characterized and analyzed with various techniques. The PAS of perovskite in different cell architectures were monitored. The evolution of the low-momentum annihilation fraction (S-parameter) as a function of positron beam energy is shown in Figure 4a. The positron distribution in the sample depends on the positron energy, which follows the Markov relation[50]

$$P(z, E) = \frac{mz^{m-1}}{z_0^m} \exp\left[-\left(\frac{z}{z_0}\right)^m\right] \tag{4}$$

where m is a constant, z is the distance to the surface, E is the positron injection energy, and z_0 is a constant and depends on the average injection depth of the positron

$$z_0 = \frac{\overline{z}}{\Gamma\left[\left(\frac{1}{m}\right) + 1\right]} \tag{5}$$

$$\overline{z} = \frac{A_{1/2}}{\rho} E^n \tag{6}$$

where Γ is the γ function, ρ is the density of the material, n and $A_{1/2}$ are constants.

According to the work of Dryzek et al.,[50] n and $A_{1/2}$ can take the value of 1.667 and 2.58 μg cm^{-2} keV^{-n}, respectively. The density of tetragonal perovskite is 4159 kg m^{-3};[51] thus, the
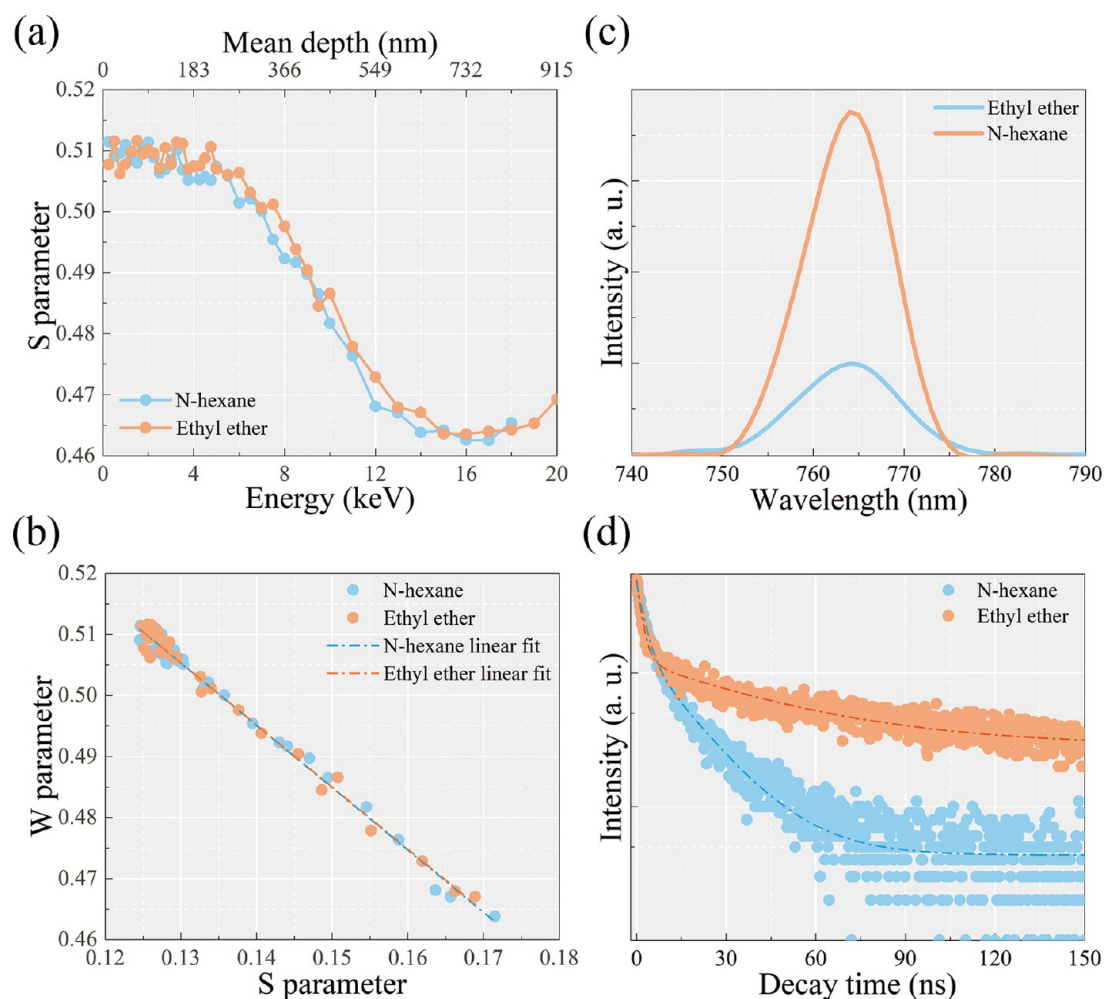
Figure 4. (a) Low-momentum annihilation fraction (*S*-parameter) vs positron beam energy for perovskite films prepared by dripping of different nonsolvents. (b) Low-momentum annihilation fraction as a function of the high-momentum annihilation fraction (*S*−*W* parameter curve) of perovskite films prepared by dripping of different nonsolvents. Emission PL spectra (c) and transient PL spectra (d) of perovskite films prepared by dripping of different nonsolvents.

Table 1. Fitting Results of Photoluminescence (PL) Decay Curves for Incomplete Ultrafast Carrier Extract Architecture (UFCEA) and Normal Structure PSCs without Back Contact

	A_e	τ_e (ns)	A_h	τ_h (ns)	A_0	τ_0 (ns)	τ_{ave} (ns)
UFCEA	137.53	0.93	276.34	4.78	82.60	21.88	14.12
normal structure	319.87	1.24	112.14	9.03	69.03	109.83	93.69

average injection depth is determined to be between 0.6 and 915.1 nm corresponding to positron energy values of 0.25 and 20 keV. In the low-positron energy range, corresponding to a shallow positron distribution depth on the surface (injection depth <200 nm), the *S*-parameter values for different perovskite films were high and at the same level. This indicates a high-surface defect density for both perovskite films. However, at the high-positron energy range, corresponding to the body of perovskite film, the *S* value of perovskite in UFCEA is lower. The *S*-parameter value revealed the lower trap density in the body of perovskite in UFCEA, which is consistent with the larger grain size. The *S*-parameter values as a function of high-momentum annihilation fractions (*W*-parameter) are plotted in Figure 4b. The *S*−*W* parameter relation reflects the defect type in the perovskite film. The simple linear relevance of *S* and *W* values without slope change denotes that only one type of defect exists for both perovskite films.[52] Positrons are mainly

captured by cation vacancies. Therefore, it is reasonable to deduce that the compact part in *n*-hexane-dripped perovskite has a lower MA⁺ vacancy density because it is reported that the organic cation migrates and escapes easily.[53,54]

The lower defect density of the perovskite layer in UFCEA is further proved by PL intensity measured on top of the glass, as presented in Figure 4c. The trap-assisted recombination in perovskite films were proven to be nonradiative.[55] In this term, perovskite films with a higher trap density yield a lower PL intensity as tremendous carriers are consumed by defects instead of direct band-gap recombination. With notably increased surface exposure, the perovskite film in UFCEA should have a high-surface defect density. However, according to the PL spectra, it in fact has a lower carrier consumption caused by nonradiative recombination.

The carrier separation rates of different device architectures were quantified with transient PL spectroscopy (Figure 4d).
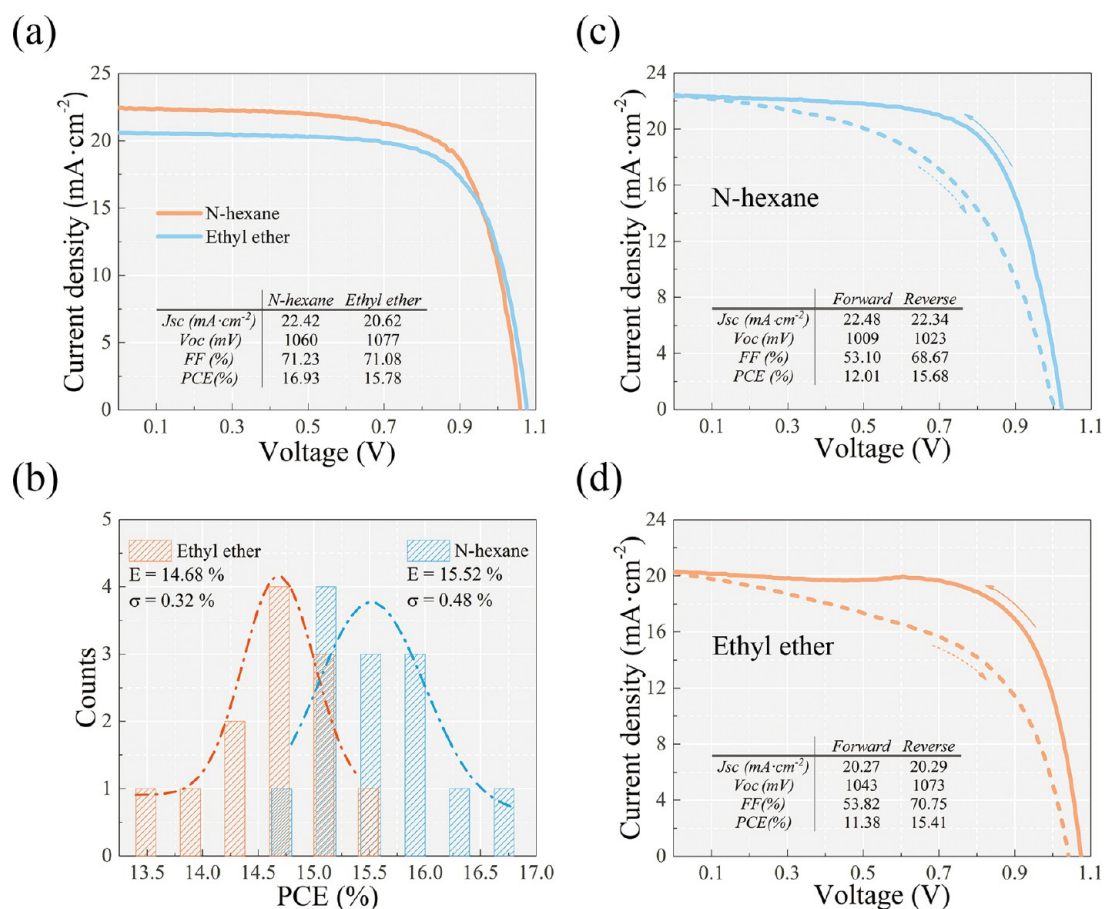
Figure 5. *J*−*V* characteristics, photovoltaic parameters (a), and efficiency histograms (b) of PSCs with UFCEA and the normal structure. Reverse and forward scan *J*−*V* characteristics of UFCEA (c) and the normal structure (d).
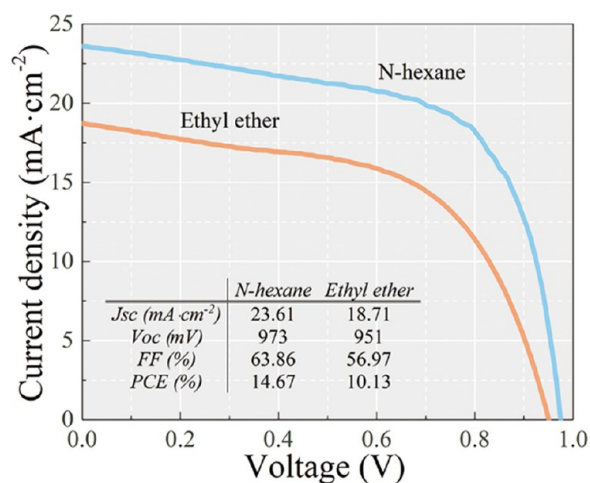
Figure 6. *J*−*V* characteristics as well as photovoltaic parameters of PSCs based on P3HT with UFCEA and the normal structure.

Incomplete devices without back contact, that is, fluorine doped tin oxide/compact TiO₂/Mesoporous TiO₂/perovskite/HTM were used to clarify the overall carrier extraction rate. The resulting PL intensity decay data are fitted with the triexponential function and are plotted as the dash dot line in Figure 4d. There are three processes that contribute to the carrier consumption: the extraction of TiO₂, the extraction of 2,2′,7,7′-tetrakis[*N,N*-di(4-methoxyphenyl)amino]-9,9′-spirobi-fluorene (Spiro-OMeTAD), and the recombination of perov-

skite. The corresponding lifetimes are denoted as τ_e, τ_h, and τ_0. The coefficients A_e, A_h, and A_0 represent the weight values of each process during the PL decay. Both the electron and hole extraction rates are faster in UFCEA compared to that of the standard configuration. It is noteworthy that not only does the hole extraction become faster in UFCEA, it also plays a more important role as the weight coefficient reveals (Table 1). The sharply decreased PL lifetime of UFCEA is hence ascribed to the difference of the perovskite/HTM interface. In both cases, the self-consumption of perovskite takes the lowest part, which ensures the high efficiency of both structures.

3.4. Device Performance and Hysteresis. The photovoltaic performance of devices with different structures was examined with Spiro-OMeTAD as HTM (Figure 5a). The UFCEA achieved a PCE of 16.93% under simulated AM 1.5 G irradiation, whereas the PCE for the standard device is 15.78%. As a result of improved light capture and interface carrier extraction, the short circuit current density (J_{SC}) is boosted from 20.62 to 22.42 mA cm⁻² and the fill factor is enhanced. A slight drop of the open circuit voltage (V_{OC}) was noticed for the device with a rough surface perovskite layer. The reason of lower V_{OC} is attributed to the larger hole transport distance in Spiro-OMeTAD in UFCEA. To verify the influence of the hole transport distance on photovoltaic performance, especially V_{OC} of PSCs, devices with different HTM thicknesses were fabricated. The *J*−*V* curves and photovoltaic characteristics are presented in Figure S2. When the HTM precursor concentration increases from 72.3 to 180 mg mL⁻¹, the V_{OC} decreases from 1072 mV to 1050 mV. Thick HTM has a high

(a)

(b)
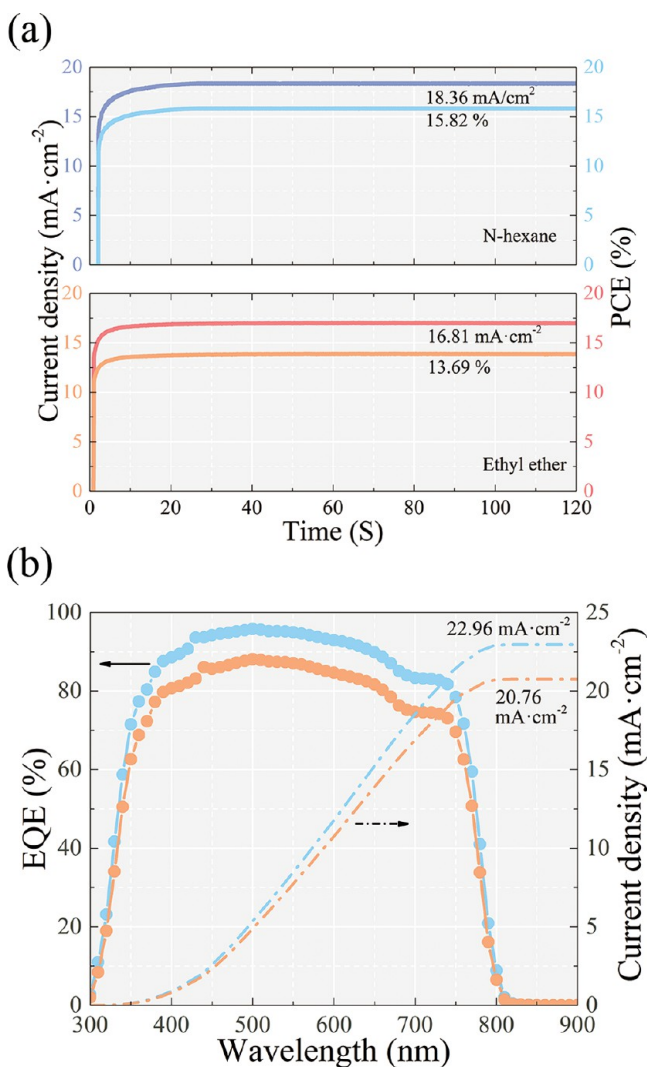
Figure 7. (a) Maximum power point tracking curve of UFCEA and the conventional structure. (b) EQE as well as integrated current density of PSCs based on UFCEA (blue) and the normal structure (orange).

hole transport loss, which affects the device performance. Although the minimum thickness of HTM (50 nm) is smaller, the maximum HTM thickness (350 nm) in UFCEA is larger than that of the traditional structure (150 nm). As the photon-generated carrier density exponentially decays from the illumination side (TiO$_2$ side), the valley of the perovskite/HTM interface (where HTM is thickest) separates most holes. As a result, the V_{OC} of UFCEA slightly drops compared to that of the normal structure. The PCEs statistics of UFCEA and the standard structure fitted with Gaussian distribution are presented in Figure 5b. According to the statistics, the PCE expectation values of UFCEA and the normal structure are 15.5 and 14.25%. The standard deviations of Gaussian curves for UFCEA and the normal structure are 0.48 and 0.32%. The inferior reproducibility of UFCEA performance might be the result of the dripping time difference as the morphology and properties of perovskite prepared with n-hexane dripping are more vulnerable to the dripping process.

The stability of PSCs with different structures was monitored. The results are provided in Figure S3. For both structures, the PCEs dramatically decreased after a storage time of 168 h. For the normal structure, 50% of initial PCE

remained, whereas a slightly lower value of 44% was observed. The stability of UFCEA is poorer. Considering that the perovskite/HTM interface area is significantly larger and a high hydrophilic additive concentration is used, it is reasonable that UFCEA degrades faster. Although the stability of UFCEA is far from the practical application threshold, it may be improved by incorporating hydrophobic HTM.

As a peculiarity of PSCs, amorphous hysteresis is a common concern. Typical J−V curves of UFCEA and the standard structure measured under different scan directions are plotted in Figure 5. The HI, denoting the percentage of accumulated power difference between reverse and forward scans was calculated. When HI is positive, the photovoltaic parameters obtained from the reverse scan curve is better, otherwise the forward scan parameter is better. The value of HI presents the extent of hysteresis; when it equals 0, no hysteresis exists. The resulting HIs are 11.95 and 14.95%, respectively, for UFCEA and the traditional structure. This reveals the hysteresis suppressing effect of UFCEA. To exclude coincidence and provide solid evidence, the HIs of eight UFCEA and normal architecture PSCs are calculated. The average value as well as the standard deviation of HI for UFCEA and standard structure PSCs are 11.29 ± 1.72 and 17.39 ± 2.14%, respectively. With UFCEA, the HI of PSCs decreased by 35.08%.

The reasons for the less significant hysteresis level or dramatically enhanced forward scan performance of UFCEA were analyzed. According to a previous report, ion migration under the electric field in perovskite results in ion redistribution.[54] The redistribution of ions induces local chemical doping. During the J−V curve test, the transient chemical doping improves the performance by increasing the built-in potential and decreasing the interface barrier. Because ions would not migrate unless the electric field applied is higher than about 0.3 V μm^{-1}, the performance of the forward scan that starts from a 0 bias is inferior. Immobilizing the ions in perovskite is conducive for suppressing hysteresis. The ion migration path is defect, vacancies, dislocations, and grain boundaries for instance. A lower defect density in n-hexane-dripped perovskite would limit the ion migration during J−V measurement. The performance enhancement effect of local chemical doping is less prominent. The enlarged perovskite/HTM interface in UFCEA also helps decrease the hysteresis level. With a larger perovskite/HTM interface, the accumulated ion population is lower.[56] The influence of transient chemical doping on photovoltaic performance is further reduced.

Although the performance improvement caused by ion migration is dramatically limited, the PCE, especially forward scan PCE of UFCEA, is notably enhanced compared to that of the normal structure. The reason of the high forward scan efficiency of UFCEA is ascribed to the shorter hole transport length in perovskite and ultrafast hole extraction. As the photon-generated carriers density has an exponential decay distribution with the distance from the illumination side (TiO$_2$ side), less holes would recombine and consume during the diffusion from the illumination side to the HTM side if the transport path is shorter. The minimum distance of HTM to mesoporous TiO$_2$ is about 250 nm in UFCEA, whereas the value in the normal structure is ~400 nm. Accordingly, the hole transport length in the perovskite layer of UFCEA decreased by 37.5%. Combined with fast carrier separation at both the electron transport material and the HTM sides, the photovoltaic performance was enhanced.
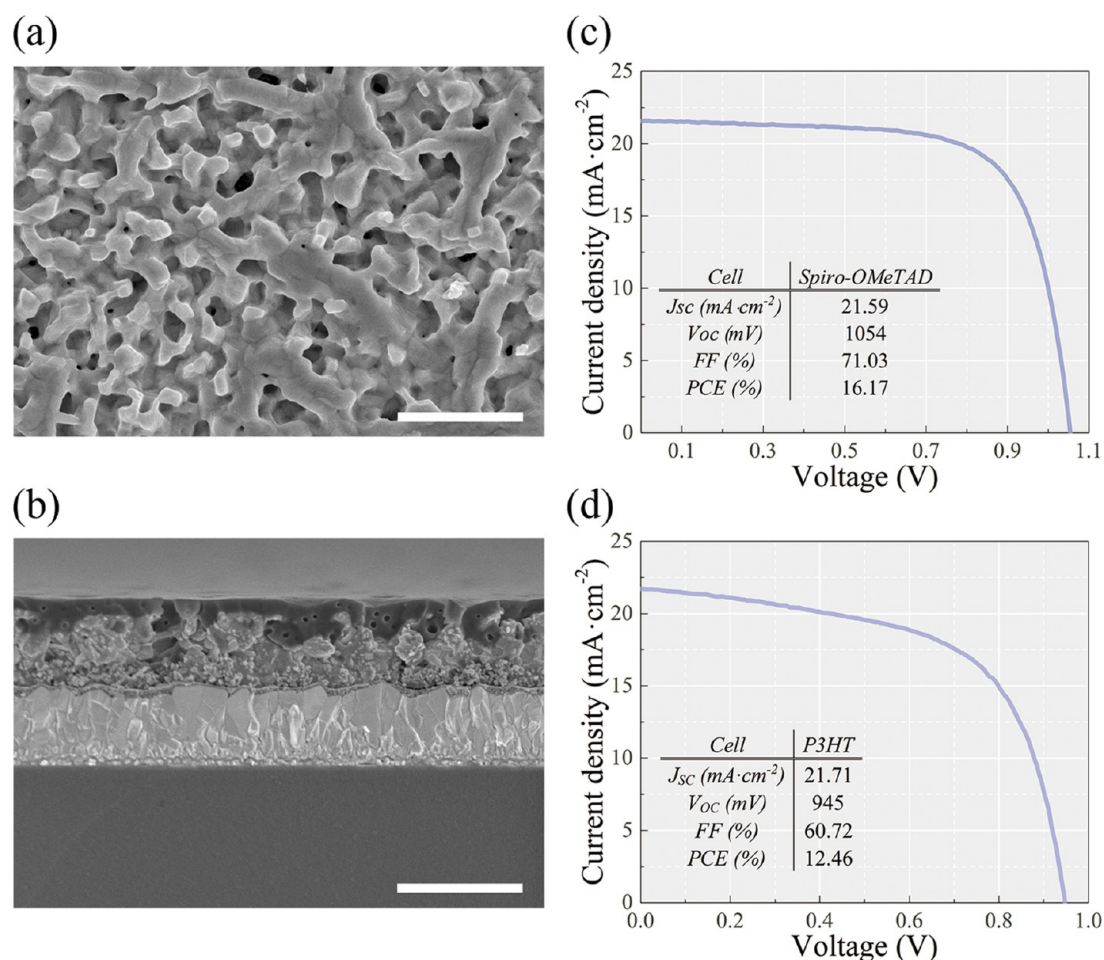
Figure 8. (a) Top-view morphology of petroleum ether-dripped perovskite on mesoporous TiO_2 and (b) cross-section morphology of Spiro-OMeTAD-coated petroleum ether-dripped perovskite on mesoporous TiO_2, the scale bars in (a) and (b) are 1 μm. $J-V$ characteristic and photovoltaic parameters of devices based on petroleum ether-dripped perovskite with (c) Spiro-OMeTAD and (d) P3HT as HTMs.

To further verify the success of UFCEA, a different HTM, poly(3-hexyl-thiophene) (P3HT), was used as the counterpart of Spiro-OMeTAD. The $J-V$ characteristics and photovoltaic parameters of P3HT-based devices are presented in Figure 6. The standard structure with a flat perovskite/P3HT interface has a PCE of 10.13%. This value increased to 14.67% with UFCEA. As far as we know, 14.67% is the highest efficiency among P3HT-based PSCs. Similar to Spiro-OMeTAD-based devices, the J_{SC} and FF of UFCEA are enhanced. In particular, the J_{SC} of P3HT-based UFCEA is boosted (with an increase of 26.2%). A PCE increase as high as 44.8% is noted, and V_{OC} is enhanced. The reason for the suitability of UFCEA especially for P3HT lies in the high hole mobility of P3HT. With a mobility of ~0.1 cm^2 V^{-1} S^{-1},[57] the transport loss in P3HT is dramatically lower compared to that in Spiro-OMeTAD (1.80 × 10^{-4} cm^2 V^{-1} S^{-1}).[58] Hence, the longer hole transport length in P3HT would not cause undesirable carrier loss. As a result, more holes are extracted from perovskite for useful work, which contributes to a higher V_{OC}.

3.5. Steady Output Curve and External Quantum Efficiency (EQE).
The validity of $J-V$ curve characterization and current density was supported by maximum power point tracking (Figure 7a) and IPCE (Figure 7b). For both device structures, the PCEs obtained from the maximum power point output curve are in consistency with the $J-V$ characteristic curve. The EQE of UFCEA is obviously higher than that of the normal device in the whole perovskite absorption range. The EQE results revealed that the light captured in UFCEA was converted to usable electricity. The integrated current densities are in good accordance with the $J-V$ characteristic curves; we thus believe our photovoltaic performance characterization results are convincing.

3.6. Morphology Formation Mechanism Analysis.
The formation of the hierarchy structure of perovskite in UFCEA was the result of the gradient supersaturation modulation effect of nonpolar solvents on perovskite precursor solution. As nonpolar solvents, n-hexane and petroleum ether for instance, are immiscible with DMF, the solute can only be precipitated at the perovskite solution/nonsolvent interface, as reported by us previously.[59,60] Although abundant nuclei form with the dripping of n-hexane, the solute does not completely precipitate from the solvent. Instead, the remaining precursor in the liquid deposit on the nuclei in the form of secondary nucleation and crystal growth with different speeds. The selective secondary nucleation on high-surface-energy sites among previously formed intermediate nuclei and crystallites contributes to the formation of nanoantennas on densely packed grains.

Except for n-hexane dripping, the morphology of perovskite prepared with petroleum ether dripping was checked. We chose petroleum ether here to confirm our hypothesis of the hierarchy perovskite formation mechanism. As a complex nonpolar solvent, petroleum ether has a similar formative

function with *n*-hexane and thus hierarchy perovskite would form if petroleum ether was dripped during the spin-coating process. As shown in the FESEM images in Figure 8a similar hierarchy perovskite was formed when *n*-hexane was replaced by petroleum ether. The distinct boundary between perovskite and HTM is observed with an irregular wave shape (Figure 8b). The photovoltaic performance of PSC based on petroleum ether-dripped perovskite is comparable to that of *n*-hexane, as indicated by the *J−V* curve and photovoltaic parameters in Figure 8c. P3HT was also used as HTM for UFCEA prepared by petroleum ether (Figure 8d). The J_{SC}, V_{OC}, FF, and PCE are 21.71 mA cm^{-2}, 945 mV, 60.72%, and 12.46%, respectively. Both Spiro-OMeTAD and P3HT UFCEA devices are less efficient when the nonsolvent is petroleum ether. The less ordered perovskite structure is believed to be the reason, as revealed by the top view and cross-section morphology. With less organized nanoantennas, the scattering effect would be weakened. This induces lower J_{SC} values of UFCEA PSC with petroleum ether compared to that with *n*-hexane. We thus suppose that with a suitable boiling point, a variety of nonpolar solvents can be used to fabricate hierarchy perovskite films that are used in UFCEA. Besides, the cell performance may be further improved by choosing a proper nonsolvent to further organize the perovskite surface.

4. CONCLUSIONS

In summary, we designed and realized a novel PSC architecture: UFCEA. UFCEA features at effective light scattering with enhanced light capture and an enlarged perovskite/HTM interface with an improved carrier separation rate. Defect study denoted that perovskite in UFCEA has a comparable surface defect density to that of perovskite in the normal structure; but in the film body, the perovskite in UFCEA has a lower defect density. With enhanced light capture and carrier extraction, Spiro-OMeTAD- and P3HT-based UFCEA PSCs achieved PCEs of 16.93 and 14.67%, respectively. The J_{SC} was dramatically enhanced. The formation mechanism of perovskite with the rough and porous surface was analyzed and verified with another nonsolvent. The fabrication process of the UFCEA PSC is not complicated; it is the same as that with the normal structure with just a replacement of the nonsolvent. The structure proposed here indicates that with the existence of a compact layer on mesoporous TiO$_2$, flat perovskite is not the single choice for high-performance PSCs. UFCEA proposed here is universal for n−i−p or p−i−n structured solar devices; with proper passivation, the photovoltaic performance would be notably improved.

■ ASSOCIATED CONTENT

ⓈSupporting Information

The Supporting Information is available free of charge on the ACS Publications website at DOI: 10.1021/acsami.7b03666.

> Detailed cell fabrication process; Tauc's plot of perovskite films in UFCEA and normal structure PSCs; *J−V* characteristics of normal structured PSCs with different HTM thicknesses; PCE evolution of UFCEA and the normal structure after a certain storage time in the dark in a dry room (PDF)

■ AUTHOR INFORMATION

Corresponding Authors
*E-mail: swyang@mail.sic.ac.cn (S.Y.).
*E-mail: liuyan@mail.sic.ac.cn (Y.L.).

ORCID ⓘ
Lei Lei: 0000-0002-0068-310X
Songwang Yang: 0000-0001-6304-5941

Author Contributions
#Y.Y. and L.L. contributed equally to this work and should be regarded as cofirst authors.

Author Contributions
The manuscript was written through contributions of all authors. All authors have given approval to the final version of the manuscript.

Notes
The authors declare no competing financial interest.

■ REFERENCES

(1) Kojima, A.; Teshima, K.; Shirai, Y.; Miyasaka, T. Organometal Halide Perovskites as Visible-Light Sensitizers for Photovoltaic Cells. *J. Am. Chem. Soc.* **2009**, *131*, 6050−6051.

(2) Best Research Cell Efficiencies, 2017. http://www.nrel.gov/ncpv/images/efficiency_chart.jpg.

(3) Kojima, A.; Ikegami, M.; Teshima, K.; Miyasaka, T. Highly Luminescent Lead Bromide Perovskite Nanoparticles Synthesized with Porous Alumina Media. *Chem. Lett.* **2012**, *41*, 397−399.

(4) Covaliu, C. I.; Chioaru, L. C.; Craciun, L.; Oprea, O.; Jitaru, I. Electrical Properties of New Organo-Inorganic Layered Perovskites. *Optoelectron. Adv. Mater., Rapid Commun.* **2011**, *5*, 1097−1102.

(5) Etgar, L.; Gao, P.; Xue, Z.; Peng, Q.; Chandiran, A. K.; Liu, B.; Nazeeruddin, M. K.; Gratzel, M. Mesoscopic CH3NH3PbI3/TiO2 Heterojunction Solar Cells. *J. Am. Chem. Soc.* **2012**, *134*, 17396−17399.

(6) Cai, B.; Xing, Y.; Yang, Z.; Zhang, W.-H.; Qiu, J. High Performance Hybrid Solar Cells Sensitized by Organolead Halide Perovskites. *Energy Environ. Sci.* **2013**, *6*, 1480−1485.

(7) Chen, Q.; Zhou, H.; Hong, Z.; Luo, S.; Duan, H.-S.; Wang, H.-H.; Liu, Y.; Li, G.; Yang, Y. Planar Heterojunction Perovskite Solar Cells via Vapor-Assisted Solution Process. *J. Am. Chem. Soc.* **2014**, *136*, 622−625.

(8) Lee, M. M.; Teuscher, J.; Miyasaka, T.; Murakami, T. N.; Snaith, H. J. Efficient Hybrid Solar Cells Based on Meso-Superstructured Organometal Halide Perovskites. *Science* **2012**, *338*, 643−647.

(9) Bisquert, J. The Swift Surge of Perovskite Photovoltaics. *J. Phys. Chem. Lett.* **2013**, *4*, 2597−2598.

(10) Stranks, S. D.; Eperon, G. E.; Grancini, G.; Menelaou, C.; Alcocer, M. J.; Leijtens, T.; Herz, L. M.; Petrozza, A.; Snaith, H. J. Electron-Hole Diffusion Lengths Exceeding 1 Micrometer in an Organometal Trihalide Perovskite Absorber. *Science* **2013**, *342*, 341−344.

(11) Xing, G.; Mathews, N.; Sun, S.; Lim, S. S.; Lam, Y. M.; Gratzel, M.; Mhaisalkar, S.; Sum, T. C. Long-Range Balanced Electron and Hole Transport Lengths in Organic-Inorganic CH$_3$NH$_3$PbI$_3$. *Science* **2013**, *342*, 344−347.

(12) Dong, Q.; Fang, Y.; Shao, Y.; Mulligan, P.; Qiu, J.; Cao, L.; Huang, J. Electron-Hole Diffusion Lengths >175 μm in Solution-Grown CH3NH3PbI3 Single Crystals. *Science* **2015**, *347*, 967−970.

(13) Rehman, W.; Milot, R. L.; Eperon, G. E.; Wehrenfennig, C.; Boland, J. L.; Snaith, H. J.; Johnston, M. B.; Herz, L. M. Charge-Carrier Dynamics and Mobilities in Formamidinium Lead Mixed-Halide Perovskites. *Adv. Mater.* **2015**, *27*, 7938−7944.

(14) Noh, J. H.; Im, S. H.; Heo, J. H.; Mandal, T. N.; Seok, S. I. Chemical Management for Colorful, Efficient, and Stable Inorganic-Organic Hybrid Nanostructured Solar Cells. *Nano Lett.* **2013**, *13*, 1764−1769.

(15) Choi, H.; Jeong, J.; Kim, H.-B.; Kim, S.; Walker, B.; Kim, G.-H.; Kim, J. Y. Cesium-doped Methylammonium Lead Iodide Perovskite Light Absorber for Hybrid Solar Cells. *Nano Energy* **2014**, *7*, 80−85.

(16) Eperon, G. E.; Stranks, S. D.; Menelaou, C.; Johnston, M. B.; Herz, L. M.; Snaith, H. J. Formamidinium Lead Trihalide: a Broadly Tunable Perovskite for Efficient Planar Heterojunction Solar Cells. *Energy Environ. Sci.* **2014**, *7*, 982−988.

(17) Hao, F.; Stoumpos, C. C.; Chang, R. P. H.; Kanatzidis, M. G. Anomalous Band Gap Behavior in Mixed Sn and Pb Perovskites Enables Broadening of Absorption Spectrum in Solar Cells. *J. Am. Chem. Soc.* **2014**, *136*, 8094−8099.

(18) Jeon, N. J.; Noh, J. H.; Yang, W. S.; Kim, Y. C.; Ryu, S.; Seo, J.; Seok, S. I. Compositional Engineering of Perovskite Materials for High-Performance Solar Cells. *Nature* **2015**, *517*, 476−480.

(19) Yang, W. S.; Noh, J. H.; Jeon, N. J.; Kim, Y. C.; Ryu, S.; Seo, J.; Seok, S. I. High-performance Photovoltaic Perovskite Layers Fabricated Through Intramolecular Exchange. *Science* **2015**, *348*, 1234−1237.

(20) Bai, S.; Cheng, N.; Yu, Z.; Liu, P.; Wang, C.; Zhao, X.-Z. Cubic: Column Composite Structure (NH2CH═NH2) × (CH3NH3)1-xPbI3 for Efficient Hole-transport Material-Free and Insulation Layer Free Perovskite Solar Cells with High Stability. *Electrochim. Acta* **2016**, *190*, 775−779.

(21) Yi, C.; Luo, J.; Meloni, S.; Boziki, A.; Ashari-Astani, N.; Gratzel, C.; Zakeeruddin, S. M.; Rothlisberger, U.; Gratzel, M. Entropic Stabilization of Mixed A-Cation ABX3 Metal Halide Perovskites for High Performance Perovskite Solar Cells. *Energy Environ. Sci.* **2016**, *9*, 656−662.

(22) Kulbak, M.; Gupta, S.; Kedem, N.; Levine, I.; Bendikov, T.; Hodes, G.; Cahen, D. Cesium Enhances Long-Term Stability of Lead Bromide Perovskite-Based Solar Cells. *J. Phys. Chem. Lett.* **2016**, *7*, 167−172.

(23) Li, Z.; Yang, M.; Park, J.-S.; Wei, S.-H.; Berry, J. J.; Zhu, K. Stabilizing Perovskite Structures by Tuning Tolerance Factor: Formation of Formamidinium and Cesium Lead Iodide Solid-State Alloys. *Chem. Mater.* **2016**, *28*, 284−292.

(24) Jesper Jacobsson, T.; Correa-Baena, J.-P.; Pazoki, M.; Saliba, M.; Schenk, K.; Gratzel, M.; Hagfeldt, A. Exploration of the Compositional Space for Mixed Lead Halogen Perovskites for High Efficiency Solar Cells. *Energy Environ. Sci.* **2016**, *9*, 1706−1724.

(25) McMeekin, D. P.; Sadoughi, G.; Rehman, W.; Eperon, G. E.; Saliba, M.; Hörantner, M. T.; Haghighirad, A.; Sakai, N.; Korte, L.; Rech, B.; Johnston, M. B.; Herz, L. M.; Snaith, H. J. A Mixed-Cation Lead Mixed-Halide Perovskite Absorber for Tandem Solar Cells. *Science* **2016**, *351*, 151−155.

(26) Zhang, W.; Anaya, M.; Lozano, G.; Calvo, M. E.; Johnston, M. B.; Míguez, H.; Snaith, H. J. Highly Efficient Perovskite Solar Cells with Tunable Structural Color. *Nano Lett.* **2015**, *15*, 1698−1702.

(27) Lu, J.-H.; Yu, Y.-L.; Chuang, S.-R.; Yeh, C.-H.; Chen, C.-P. High-Performance, Semitransparent, Easily Tunable Vivid Colorful Perovskite Photovoltaics Featuring Ag/ITO/Ag Microcavity Structures. *J. Phys. Chem. C* **2016**, *120*, 4233−4239.

(28) Kim, H. S.; Lee, C. R.; Im, J. H.; Lee, K. B.; Moehl, T.; Marchioro, A.; Moon, S. J.; Humphry-Baker, R.; Yum, J. H.; Moser, J. E.; Gratzel, M.; Park, N. G. Lead Iodide Perovskite Sensitized All-Solid-State Submicron Thin Film Mesoscopic Solar Cell with Efficiency Exceeding 9%. *Sci. Rep.* **2012**, *2*, No. 591.

(29) Burschka, J.; Pellet, N.; Moon, S. J.; Humphry-Baker, R.; Gao, P.; Nazeeruddin, M. K.; Gratzel, M. Sequential Deposition As a Route to High-Performance Perovskite-Sensitized Solar Cells. *Nature* **2013**, *499*, 316−319.

(30) Xiao, M.; Huang, F.; Huang, W.; Dkhissi, Y.; Zhu, Y.; Etheridge, J.; Gray-Weale, A.; Bach, U.; Cheng, Y.-B.; Spiccia, L. A Fast Deposition-Crystallization Procedure for Highly Efficient Lead Iodide Perovskite Thin-Film Solar Cells. *Angew. Chem., Int. Ed.* **2014**, *53*, 9898−9903.

(31) Jeon, N. J.; Noh, J. H.; Kim, Y. C.; Yang, W. S.; Ryu, S.; Seok, S. I. Solvent Engineering for High-Performance Inorganic-organic Hybrid Perovskite Solar Cells. *Nat. Mater.* **2014**, *13*, 897−903.

(32) Zhou, Y.; Yang, M.; Wu, W.; Vasiliev, A. L.; Zhu, K.; Padture, N. P. Room-Temperature Crystallization of Hybrid-Perovskite Thin Films Via Solvent-Solvent Extraction for High-Performance Solar Cells. *J. Mater. Chem. A* **2015**, *3*, 8178−8184.

(33) Pan, J.; Mu, C.; Li, Q.; Li, W.; Ma, D.; Xu, D. Room-Temperature, Hydrochloride-Assisted, One-Step Deposition for Highly Efficient and Air-Stable Perovskite Solar Cells. *Adv. Mater.* **2016**, *28*, 8309−8314.

(34) Tao, C.; Neutzner, S.; Colella, L.; Marras, S.; Srimath Kandada, A. R.; Gandini, M.; Bastiani, M. D.; Pace, G.; Manna, L.; Caironi, M.; Bertarelli, C.; Petrozza, A. 17.6% Stabilized Efficiency in Low-Temperature Processed Planar Perovskite Solar Cells. *Energy Environ. Sci.* **2015**, *8*, 2365−2370.

(35) Ahn, N.; Son, D.-Y.; Jang, I.-H.; Kang, S. M.; Choi, M.; Park, N.-G. Highly Reproducible Perovskite Solar Cells with Average Efficiency of 18.3% and Best Efficiency of 19.7% Fabricated via Lewis Base Adduct of Lead(II) Iodide. *J. Am. Chem. Soc.* **2015**, *137*, 8696−8699.

(36) Liu, M.; Johnston, M. B.; Snaith, H. J. Efficient Planar Heterojunction Perovskite Solar Cells by Vapour Deposition. *Nature* **2013**, *501*, 395−398.

(37) Huang, F.; Dkhissi, Y.; Huang, W.; Xiao, M.; Benesperi, I.; Rubanov, S.; Zhu, Y.; Lin, X.; Jiang, L.; Zhou, Y.; Gray-Weale, A.; Etheridge, J.; McNeill, C. R.; Caruso, R. A.; Bach, U.; Spiccia, L.; Cheng, Y.-B. Gas-Assisted Preparation of Lead Iodide Perovskite Films Consisting of a Monolayer of Single Crystalline Grains for High Efficiency Planar Solar Cells. *Nano Energy* **2014**, *10*, 10−18.

(38) Wang, D.; Liu, Z.; Zhou, Z.; Zhu, H.; Zhou, Y.; Huang, C.; Wang, Z.; Xu, H.; Jin, Y.; Fan, B.; Pang, S.; Cui, G. Reproducible One-Step Fabrication of Compact MAPbI3−xClx Thin Films Derived from Mixed-Lead-Halide Precursors. *Chem. Mater.* **2014**, *26*, 7145−7150.

(39) Lv, S.; Pang, S.; Zhou, Y.; Padture, N. P.; Hu, H.; Wang, L.; Zhou, X.; Zhu, H.; Zhang, L.; Huang, C.; Cui, G. One-Step, Solution-Processed Formamidinium Lead Trihalide (FAPbI(3-x)Clx) for Mesoscopic Perovskite-Polymer Solar Cells. *Phys. Chem. Chem. Phys.* **2014**, *16*, 19206−19211.

(40) Li, X.; Bi, D.; Yi, C.; Décoppet, J.-D.; Luo, J.; Zakeeruddin, S. M.; Hagfeldt, A.; Grätzel, M. A Vacuum Flash-Assisted Solution Process for High-Efficiency Large-Area Perovskite Solar Cells. *Science* **2016**, *353*, 58−62.

(41) Im, J.-H.; Jang, I.-H.; Pellet, N.; Grätzel, M.; Park, N.-G. Growth of CH3NH3PbI3 Cuboids with Controlled Size for High-Efficiency Perovskite Solar Cells. *Nat. Nanotechnol.* **2014**, *9*, 927−932.

(42) Yang, W. S.; Noh, J. H.; Jeon, N. J.; Kim, Y. C.; Ryu, S.; Seo, J.; Seok, S. I. High-Performance Photovoltaic Perovskite Layers Fabricated Through Intramolecular Exchange. *Science* **2015**, *348*, 1234−1237.

(43) Ji, F.; Wang, L.; Pang, S.; Gao, P.; Xu, H.; Xie, G.; Zhang, J.; Cui, G. A Balanced Cation Exchange Reaction toward Highly Uniform and Pure Phase FA1-xMAxPbI3 Perovskite Films. *J. Mater. Chem. A* **2016**, *4*, 14437−14443.

(44) Zhou, Z.; Pang, S.; Ji, F.; Zhang, B.; Cui, G. The Fabrication of Formamidinium Lead Iodide Perovskite Thin Films Via Organic Cation Exchange. *Chem. Commun.* **2016**, *52*, 3828−3831.

(45) Zhou, Y.; Yang, M.; Pang, S.; Zhu, K.; Padture, N. P. Exceptional Morphology-Preserving Evolution of Formamidinium Lead Triiodide Perovskite Thin Films via Organic-Cation Displacement. *J. Am. Chem. Soc.* **2016**, *138*, 5535−5538.

(46) Chen, S.; Lei, L.; Yang, S.; Liu, Y.; Wang, Z.-S. Characterization of Perovskite Obtained from Two-Step Deposition on Mesoporous Titania. *ACS Appl. Mater. Interfaces* **2015**, *7*, 25770−25776.

(47) Li, W.; Fan, J.; Li, J.; Mai, Y.; Wang, L. Controllable Grain Morphology of Perovskite Absorber Film by Molecular Self-Assembly toward Efficient Solar Cell Exceeding 17%. *J. Am. Chem. Soc.* **2015**, *137*, 10399−10405.

(48) Bi, D.; Tress, W.; Dar, M. I.; Gao, P.; Luo, J.; Renevier, C.; Schenk, K.; Abate, A.; Giordano, F.; Correa Baena, J.-P.; Decoppet, J.-D.; Zakeeruddin, S. M.; Nazeeruddin, M. K.; Grätzel, M.; Hagfeldt, A. Efficient Luminescent Solar Cells Based on Tailored Mixed-Cation Perovskites. *Sci. Adv.* **2016**, *2*, No. 23151170.

(49) Saliba, M.; Matsui, T.; Seo, J.-Y.; Domanski, K.; Correa-Baena, J.-P.; Nazeeruddin, M. K.; Zakeeruddin, S. M.; Tress, W.; Abate, A.; Hagfeldt, A.; Gratzel, M. Cesium-Containing Triple Cation Perovskite Solar Cells: Improved Stability, Reproducibility and High Efficiency. *Energy Environ. Sci.* **2016**, *9*, 1989−1997.

(50) Dryzek, J.; Dryzek, E.; Börner, F.; Krause-Rehberg, R. Subsurface Zones Created Under Lubrication Conditions Studied by Positron Annihilation. *Tribol. Lett.* **2001**, *11*, 29−36.

(51) Stoumpos, C. C.; Malliakas, C. D.; Kanatzidis, M. G. Semiconducting Tin and Lead Iodide Perovskites with Organic Cations: Phase Transitions, High Mobilities, and Near-Infrared Photoluminescent Properties. *Inorg. Chem.* **2013**, *52*, 9019−9038.

(52) Ergen, O.; Gilbert, S. M.; Pham, T.; Turner, S. J.; Tan, M. T. Z.; Worsley, M. A.; Zettl, A. Graded Bandgap Perovskite Solar Cells. *Nat. Mater.* **2017**, *16*, 522−525.

(53) De Bastiani, M.; Dell'Erba, G.; Gandini, M.; D'Innocenzo, V.; Neutzner, S.; Kandada, A. R. S.; Grancini, G.; Binda, M.; Prato, M.; Ball, J. M.; Caironi, M.; Petrozza, A. Ion Migration and the Role of Preconditioning Cycles in the Stabilization of the J-V Characteristics of Inverted Hybrid Perovskite Solar Cells. *Adv. Energy Mater.* **2016**, *6*, No. 1501453.

(54) Yuan, Y.; Huang, J. Ion Migration in Organometal Trihalide Perovskite and Its Impact on Photovoltaic Efficiency and Stability. *Acc. Chem. Res.* **2016**, *49*, 286−293.

(55) Wetzelaer, G.-J. A. H.; Scheepers, M.; Sempere, A. M.; Momblona, C.; Ávila, J.; Bolink, H. J. Trap-Assisted Non-Radiative Recombination in Organic-Inorganic Perovskite Solar Cells. *Adv. Mater.* **2015**, *27*, 1837−1841.

(56) Huang, A.; Lei, L.; Zhu, J.; Yu, Y.; Liu, Y.; Yang, S.; Bao, S.; Jin, P. Controllable Deposition of TiO_2 Nanopillars at Room Temperature for High Performance Perovskite Solar Cells with Suppressed Hysteresis. *Sol. Energy Mater. Sol. Cells* **2017**, *168*, 172−182.

(57) Chang, J.-F.; Sun, B.; Breiby, D. W.; Nielsen, M. M.; Sölling, T. I.; Giles, M.; McCulloch, I.; Sirringhaus, H. Enhanced Mobility of Poly(3-hexylthiophene) Transistors by Spin-Coating from High-Boiling-Point Solvents. *Chem. Mater.* **2004**, *16*, 4772−4776.

(58) Reddy, S. S.; Gunasekar, K.; Heo, J. H.; Im, S. H.; Kim, C. S.; Kim, D.-H.; Moon, J. H.; Lee, J. Y.; Song, M.; Jin, S.-H. Highly Efficient Organic Hole Transporting Materials for Perovskite and Organic Solar Cells with Long-Term Stability. *Adv. Mater.* **2016**, *28*, 686−693.

(59) Yu, Y.; Yang, S.; Lei, L.; Liu, Y. Nucleation Mediated Interfacial Precipitation for Architectural Perovskite Films with Enhanced Photovoltaic Performance. *Nanoscale* **2017**, *9*, 2569−2578.

(60) Yu, Y.; Yang, S.; Lei, L.; Cao, Q.; Shao, J.; Zhang, S.; Liu, Y. Ultrasmooth Perovskite Film via Mixed Anti-Solvent Strategy with Improved Efficiency. *ACS Appl. Mater. Interfaces* **2017**, *9*, 3667−3676.